arXiv:1402.5983v1 [quant-ph] 24 Feb 2014

Quantum noise in large-scale coherent nonlinear photonic circuits

Charles Santori, Jason S. Pelc, and Raymond G. Beausoleil
Hewlett-Packard Laboratories, 1501 Page Mill Road, MS1123, Palo Alto, California 94304, USA

Nikolas Tezak, Ryan Hamerly, and Hideo Mabuchi
Edward L. Ginzton Laboratory, Stanford University, Stanford, CA 94305, USA

A semiclassical simulation approach is presented for studying quantum noise in large-scale photonic circuits incorporating an ideal Kerr nonlinearity. A netlist-based circuit solver is used to generate matrices defining a set of stochastic differential equations, in which the resonator field variables represent random samplings of the Wigner quasi-probability distributions. Although the semiclassical approach involves making a large-photon-number approximation, tests on one- and two-resonator circuits indicate satisfactory agreement between the semiclassical and full-quantum simulation results in the parameter regime of interest. The semiclassical model is used to simulate random errors in a large-scale circuit that contains 88 resonators and hundreds of components in total, and functions as a 4-bit ripple counter. The error rate as a function of on-state photon number is examined, and it is observed that the quantum fluctuation amplitudes do not increase as signals propagate through the circuit, an important property for scalability.

PACS numbers: 42.50.Lc, 42.65.Pc

I. INTRODUCTION

While all-optical logic has historically been difficult to implement [1], recent progress in micro- and nano-scale optical devices has renewed interest in this subject, as it could allow pushing energy consumption to regimes that have not been attainable in bulk optical systems. In room-temperature experiments, carrier-based optical switching has been demonstrated at 100 fJ pulse energies in silicon devices [2] and at sub-fJ pulse energies in devices made from III-V materials [3], where bistable optical memories have also been implemented [4]. Switching based on far-off-resonant (Kerr) nonlinearities typically requires higher powers, but has been demonstrated at < 1 pJ in ring resonators made from amorphous silicon [5]. In low-temperature experiments, fJ-scale optical logic has been achieved in exciton-polariton systems [6], and switching near the single-photon level has been achieved in quantum dots coupled to photonic-crystal resonators[7, 8]. Low-temperature atomic ensembles can also be used quite effectively for low-photon-number switching [9, 10]. Thus, low-temperature switching experiments are already well into regimes where quantum effects are important for the switching dynamics [11], and room-temperature devices may soon reach such regimes, as well.

Simulation tools are therefore needed that can predict quantum effects in the $\sim 10 - 1000$ photon regime, such as random error rates due to quantum jumps, and new types of behavior that might occur when many components interact through coherent signals. Full-quantum simulation methods, such as the SLH model [12] and QHDL [13] may be used to study circuits containing 1-3 idealized components, but the exponential scaling of the state space with respect to the number of resonators requires some kind of approximation to be made before larger circuits can be studied [13–16].

Here, we describe semiclassical simulations following a method that can be applied to large-scale networks of Kerr-nonlinear resonators connected through linear optics. The stochastic differential equations we use are similar to equations used previously [17], with the dynamic field variables representing a random sampling of the Wigner quasi-probability distribution. However, this is the first demonstration, to our knowledge, of combining such a model with a circuit solver that automatically converts a netlist, which describes an optical circuit topology, into a set of matrices representing the stochastic differential equations. This allows us to construct large circuits based on multiple layers of subcircuits, such as the 4-bit ripple counter described below. The computation time scales polynomially with the number of components, and in many circuits the scaling is approximately linear. Even though our model uses just one complex variable to describe each resonator, for the parameter regime of interest, we can reproduce the spontaneous switching events in one- or two-element circuits predicted by a full-quantum simulation. When the noise terms are removed, our model is the same as coupled mode theory [18] (with energy scaled in photon units), and thus the same tool can be used to perform classical simulations. Our results indicate that a pure Kerr nonlinearity, combined with auxiliary coherent inputs, can be used to create arbitrary logic, with tolerance to moderate linear loss, and adequate signal restoration for cascading. Such circuits can function with negligible errors at intra-cavity energies down to a few tens of attojoules.

II. SIMULATION METHOD

Suppose we have an optical circuit consisting of a set of nonlinear resonators connected by linear optical components, including waveguides, beamsplitters and phase

shifters, and driven by coherent external inputs. When simulating such a circuit we will be interested in characterizing both its internal state as well as the resulting output fields. In modeling the internal state we will only keep track of long-lived resonator modes within the photonic structure and assume that the fields propagating in the interconnecting waveguides can always be described in terms of these resonator modes and the input fields at the same instant in time. Modeling the full dynamics of the waveguide modes would make a computational treatment much more difficult, and for circuits with dynamics on timescales much longer than it takes light to propagate across the structure (on the order of picoseconds for integrated optical circuits), it is reasonable to assume instantaneous light propagation between resonators.

In Section II A we will introduce the final dynamical model which we use to simulate circuits. Since we are interested in operating at fairly low light intensities, quantum shot noise can play an important role in the dynamics. Therefore our model is of a stochastic nature: Both the resonator fields as well as the inputs and outputs are taken to be stochastic processes. We will show how these equations can be derived from a Fokker-Planck equation for the Wigner quasi-probability distribution of our quantum optical circuit model in II B, and we show how these circuit models can be obtained from their component models in II C. Finally, in II D we discuss the software and numerical implementation of our model, and compare results obtained from our model with those obtained by carrying out full quantum simulations.

A. Equations

In our description of photonic circuits we clearly distinguish between the electro-magnetic modes $\{a_j\}$ associated with high-Q optical resonators and the propagating field modes $\{b_k(\omega)\}$ of the connecting waveguides. While the resonator modes are discrete, the waveguides modes have a continuous spectrum. This results in the different commutator relationships: $[a_j, a_k^\dagger] = \delta_{jk}$ vs. $[b_j(\omega), b_k(\omega')] = \delta_{jk}\delta(\omega-\omega')$ and, in correspondence with these, different physical units. Instead of keeping track of the full spatio-temporal dynamics of waveguide modes we will exploit the small spatial dimension of the systems under consideration and simply keep track of input and output amplitudes of the overall system. Formally, we would now proceed by introducing input and output mode operators $b_{\mathrm{in},k}(t)$ and $b_{\mathrm{out},k}(t)$ as linear combinations of the waveguide mode operators before and after the interaction with the circuit. This leads to the input-output formalism in quantum optics [19, 20]. The main result of that formalism relevant to this work is how input and output fields are related to each other and the scattering system. For a single waveguide coupled to a system via a Heisenberg-picture coupling operator $L(t)$, the input output relation is given as $b_{\mathrm{out}}(t) = b_{\mathrm{in}}(t) + L(t)$. We will later generalize this to systems involving multiple inputs and outputs with non-trivial scattering between them.

Throughout this work we denote the time-dependent complex resonator mode amplitudes as $\alpha_j(t) \leftrightarrow a_j(t)$, the coherent input signal amplitudes as $\beta_{\mathrm{in},k}(t) \leftrightarrow b_{\mathrm{in},k}(t)$ and the output signals as $\beta_{\mathrm{out},l}(t) \leftrightarrow b_{\mathrm{out},l}(t)$. The notation here should be understood to imply that taking the ensemble average of the stochastic variables on the left hand side equals taking the quantum mechanical expectation value of the right hand side.

In the following sections we will derive stochastic differential equations (SDEs) for the resonator mode amplitudes both for single systems and circuits composed of such systems. The most important resonator model for this work is given by a Kerr-nonlinear resonator with multiple input/output couplings. Its SDE is given by

$$\dot{\alpha}(t) = -\left[\frac{\kappa}{2} + i\Delta + 2i\chi(\alpha^*\alpha - 1)\right]\alpha - \sum_j \sqrt{\kappa_j} e^{-i\psi_j}\beta_{\mathrm{in},j}(t) \tag{1}$$

$$\beta_{\mathrm{out},j}(t) = \sqrt{\kappa_j} e^{i\psi_j}\alpha(t) + \beta_{\mathrm{in},j}(t) \tag{2}$$

Here κ_j are the coupling rates between the resonator and the waveguides, $\kappa = \sum_j \kappa_j$ is the total decay rate, ψ_j are coupling phases, Δ is the resonator detuning from a reference frequency, and χ is the nonlinearity. The input field $\beta_{\mathrm{in},j}(t) = \bar{\beta}_{\mathrm{in},j}(t) + \eta_j(t)$ can be separated explicitly into a deterministic coherent amplitude $\bar{\beta}_{\mathrm{in},j}(t)$ and a stochastic part $\eta_j(t) = \eta_j^{(1)}(t) + i\eta_j^{(2)}$ which we assume to be independent complex gaussian noise processes with zero mean $\langle \eta_j(t) \rangle = 0$ and second-order moments $\langle \eta_j^{(m)}(t)\eta_j^{(n)}(t') \rangle = \frac{1}{4}\delta_{jk}\delta_{mn}\delta(t-t')$. These equations of motion are thus a system of Langevin equations, i.e. stochastic differential equations, but since the coefficients to the noise terms are state independent, they assume the same form in both the Ito and Stratonovich convention.

It is important to note that although the internal mode variables have nonlinear equations of motion, the coupling to the external inputs and noises is fully linear. This makes it straightforward to derive rules for how to combine such systems into a circuit.

B. Derivation

Equations (1) - (2) can be derived from a Fokker-Planck equation for the overall system's Wigner quasi-probability distribution. In the following, we start by deriving the Fokker-Planck equation for a single-mode Kerr-nonlinear optical resonator to demonstrate the basic procedure and then proceed to generalize this to networks of multi-mode Kerr-nonlinear resonators.

1. Single-mode resonator model

We start with the simplest open-system Kerr-nonlinear resonator model featuring a single mode and a single dissipative coupling to an external field in the vacuum. This system is described by a Hamiltonian H and a single collapse operator L given by

$$H = \Delta a^\dagger a + \chi a^{\dagger 2} a^2 \tag{3}$$
$$L = \sqrt{\kappa} e^{i\psi} a. \tag{4}$$

L is the Lindblad-collapse operator [21] associated with photon leakage out of the resonator at a rate κ. The corresponding Lindblad-Master equation is then given by

$$\dot{\rho} = -i[H,\rho] + L\rho L^\dagger - \frac{1}{2}\left(L^\dagger L\rho + \rho L^\dagger L\right), \tag{5}$$

consisting of the usual coherent part $-i[H,\rho]$ and the dissipative part $\mathcal{D}[L]\rho := L\rho L^\dagger - \frac{1}{2}\left[L^\dagger L\rho + \rho L^\dagger L\right]$.

The well-known Wigner transform of an oscillator state ρ is given by [22]

$$\mathcal{W}\{\rho\}(\alpha,\alpha^*) := \frac{1}{\pi^2}\int d^2\beta e^{-i\beta\alpha^* - i\beta^*\alpha}\mathrm{Tr}\left(e^{i\beta a^\dagger + i\beta^* a}\rho\right), \tag{6}$$

and from this we define the system's Wigner function as $W(\alpha,\alpha^*,t) := \mathcal{W}\{\rho(t)\}$. To find out how the Wigner function evolves in time, we differentiate and substitute in the Master equation

$$\partial_t W(\alpha,\alpha^*,t) = \mathcal{W}\left\{\frac{d}{dt}\rho\right\} = \mathcal{W}\left\{-i[H,\rho]\right\} + \mathcal{W}\left\{\mathcal{D}[L]\rho\right\}.$$

The Wigner distribution is useful because of the correspondence between quantum expectation values for mode operator moments and its moments, e.g.

$$\langle a\rangle = \langle\alpha\rangle_W, \tag{7}$$
$$\langle a^\dagger\rangle = \langle\alpha^*\rangle_W, \tag{8}$$
$$\langle n\rangle = \langle a^\dagger a\rangle = \langle\alpha^*\alpha\rangle_W - \frac{1}{2}, \tag{9}$$
$$\mathrm{Var}(n) = \langle(n-\langle n\rangle)^2\rangle = \mathrm{Var}(\alpha^*\alpha)_W - \frac{1}{4} \tag{10}$$
$$\mathrm{Var}\left(\frac{a+a^\dagger}{2}\right) = \mathrm{Var}\left(\frac{\alpha+\alpha^*}{2}\right)_W. \tag{11}$$

This means that instead of performing a full quantum simulation to evaluate operator expectation values, we can instead sample directly from the Wigner-distribution.

A few calculations [17] show that

$$\mathcal{W}\{a\rho\} = \left(\alpha + \frac{\partial_{\alpha^*}}{2}\right)\mathcal{W}\{\rho\}, \quad \mathcal{W}\{\rho a\} = \left(\alpha - \frac{\partial_{\alpha^*}}{2}\right)\mathcal{W}\{\rho\},$$
$$\mathcal{W}\{a^\dagger\rho\} = \left(\alpha^* - \frac{\partial_\alpha}{2}\right)\mathcal{W}\{\rho\}, \quad \mathcal{W}\{\rho a^\dagger\} = \left(\alpha^* + \frac{\partial_\alpha}{2}\right)\mathcal{W}\{\rho\},$$

and these relations can be iterated to yield

$$\begin{aligned}
\mathcal{W}\{[a^\dagger a,\rho]\} &= \left(\partial_{\alpha^*}\alpha^* - \partial_\alpha\alpha\right)\mathcal{W}\{\rho\},\\
\mathcal{W}\{[a^{\dagger 2}a^2,\rho]\} &= 2[\partial_{\alpha^*}(\alpha^*\alpha-1)\alpha^* - \partial_\alpha(\alpha^*\alpha-1)\alpha\\
&\quad + \frac{1}{4}\partial_\alpha^2\partial_{\alpha^*}\alpha - \frac{1}{4}\partial_{\alpha^*}^2\partial_\alpha\alpha^*]\mathcal{W}\{\rho\},\\
\mathcal{W}\{\mathcal{D}[a]\rho\} &= \frac{1}{2}\left[\partial_{\alpha^*}\alpha^* + \partial_\alpha\alpha + \partial_{\alpha^*}\partial_\alpha\right]\mathcal{W}\{\rho\},
\end{aligned}$$

such that we ultimately find

$$\begin{aligned}
\partial_t\mathcal{W} = &-i\Delta\left(\partial_{\alpha^*}\alpha^* - \partial_\alpha\alpha\right)\mathcal{W}\\
&- i\chi\left(\partial_{\alpha^*}(\alpha^*\alpha-1)\alpha^* - \partial_\alpha(\alpha^*\alpha-1)\alpha\right)\mathcal{W}\\
&- i\chi\left(\frac{1}{4}\partial_\alpha^2\partial_{\alpha^*}\alpha - \frac{1}{4}\partial_{\alpha^*}^2\partial_\alpha\alpha^*\right)\mathcal{W}\\
&+ \frac{\kappa}{2}\left(\partial_\alpha\alpha + \partial_{\alpha^*}\alpha^* + \partial_{\alpha^*}\partial_\alpha\right)\mathcal{W}.
\end{aligned} \tag{12}$$

As discussed in Ref. [17], in order to arrive at proper Fokker-Planck equations, we must drop the third-order derivatives, i.e. the third row in Equation (12). This is justified in the case of large photon numbers in the resonators, since, assuming $\partial_\alpha \sim 1$, the first-derivative terms containing χ are a factor of $\sim |\alpha|^2$ larger. The resulting Langevin equation for $\alpha(t)$ is then given by

$$\dot{\alpha}(t) = -\left[\frac{\kappa}{2} + i\Delta + i\chi\left(\alpha^*(t)\alpha(t) - 1\right)\right]\alpha(t) - \sqrt{\kappa}\beta_{\mathrm{in}}(t) \tag{13}$$

where the expression in brackets corresponds to first-derivative (drift) terms in the Fokker-Planck equation, and the noise term on the right corresponds to the second-derivative (diffusion) term. So far our system is driven only by a vacuum input and we have not shown how to obtain the output of the system. The output process of this undriven system is given by

$$\beta_{\mathrm{out}}(t) = \sqrt{\kappa}\alpha(t) + \beta_{\mathrm{in}}(t). \tag{14}$$

The process $\beta_{\mathrm{in}}(t)$ in Equations (13) and (14) is the input field. For a vacuum input, this is a complex Wiener process $\beta_{\mathrm{in}}(t) = \eta^{(1)}(t) + i\eta^{(2)}(t)$, with $\langle\eta^{(m)}(t)\eta^{(n)}(t')\rangle = \frac{1}{4}\delta_{mn}\delta(t-t')$. This noise term captures the quantum shot noise of the input field. Driving the resonator with a coherent field is done by displacing the vacuum input process $\beta_{\mathrm{in}}(t) \to \bar{\beta}_{\mathrm{in}}(t) + \eta(t)$, where $\bar{\beta}_{\mathrm{in}}(t)$ is a complex-valued, deterministic function of time.

2. Single-mode resonator with multiple inputs and outputs

With the above work, the generalization to multiple inputs and outputs is straightforward. We thus assume

a Hamiltonian and vector of collapse operators

$$H = \Delta a^\dagger a + \frac{\chi}{2} a^{\dagger 2} a^2 \tag{15}$$

$$\mathbf{L} = \begin{pmatrix} \sqrt{\kappa_1} e^{i\psi_1} a \\ \sqrt{\kappa_2} e^{i\psi_2} a \\ \vdots \\ \sqrt{\kappa_n} e^{i\psi_n} a \end{pmatrix} \tag{16}$$

where we have allowed for different phases associated with each input port. Inserting these into the Lindblad master equation:

$$\dot{\rho} = -i[H, \rho] + \sum_{k=1}^{n} \mathcal{D}[L_k]\rho, \tag{17}$$

leads to the SDE in Eqs. (1) - (2).

3. *Static Components*

Three static components are needed – a beamsplitter, a phase shifter and a coherent displacement. These components do not have internal states; their input-output relations are fully described by a scattering matrix. For the beamsplitter, which is parameterized by an angle θ:

$$\begin{bmatrix} \beta_{\text{out},1}(t) \\ \beta_{\text{out},2}(t) \end{bmatrix} = \begin{bmatrix} \cos\theta & -\sin\theta \\ \sin\theta & \cos\theta \end{bmatrix} \begin{bmatrix} \beta_{\text{in},1}(t) \\ \beta_{\text{in},2}(t) \end{bmatrix} \tag{18}$$

A phase shifter is parameterized by a phase ϕ:

$$\beta_{\text{out}} = e^{i\phi} \beta_{\text{in}} \tag{19}$$

A coherent displacement is parameterized by a displacement field β_0, which adds to the current field. This is equivalent to bouncing light off a highly reflective beamsplitter with a very strong field entering through the dark port:

$$\beta_{\text{out}} = \beta_{\text{in}} + \beta_0 \tag{20}$$

C. Circuits of Components

Stochastic equations for circuits of many components can be obtained in a straightforward, algorithmic manner. First, the input-output equations for each component $\mathcal{K}^{(i)}$ are written down in the following general form:

$$\begin{aligned} \dot{\alpha}^{(i)}(t) &= \left[\mathbf{A}^{(i)}\alpha^{(i)}(t) + \mathbf{a}^{(i)} + A_{\text{NL}}^{(i)}(\alpha^{(i)}, t)\right] + \mathbf{B}^{(i)}\beta_{\text{in}}^{(i)}(t) \\ \beta_{\text{out}}^{(i)}(t) &= \left[\mathbf{C}^{(i)}\alpha^{(i)}(t) + \mathbf{c}^{(i)}\right] + \mathbf{D}^{(i)}\beta_{\text{in}}^{(i)}(t) \end{aligned} \tag{21}$$

where i is the component index, $\alpha^{(i)}(t)$ is a vector of field amplitudes for all resonators belonging to $\mathcal{K}^{(i)}$; $\beta_{\text{in}}^{(i)}(t)$ and $\beta_{\text{out}}^{(i)}(t)$ are vectors of inputs and outputs to $\mathcal{K}^{(i)}$, $\mathbf{A}, \mathbf{B}, \mathbf{C}$, and $\mathbf{D}$ are constant matrices, and $\mathbf{a}$ and $\mathbf{c}$ are constant vectors. For static components, only $\mathbf{D}$ and $\mathbf{c}$ are defined, the rest of the matrices and vectors being ignored because the component has no internal state.

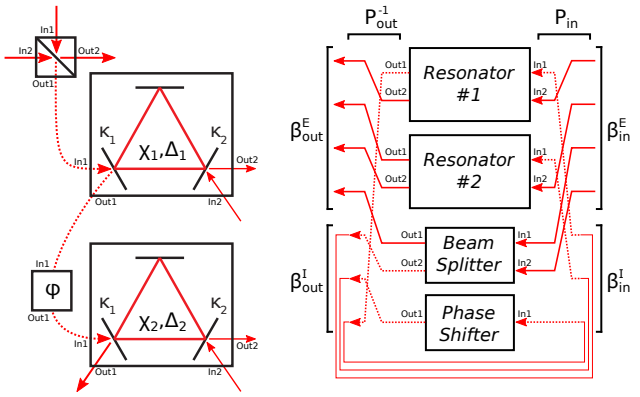

FIG. 1: Example circuit showing external $(\beta_{\text{out}}^E, \beta_{\text{in}}^E)$ and internal $(\beta_{\text{out}}^I, \beta_{\text{in}}^I)$ input-output fields.

A circuit consists of many such components $(\mathcal{K}^{(1)}, \ldots, \mathcal{K}^{(n)})$, connected together, meaning that $\beta_{\text{in},m}^{(i)}(t) = \beta_{\text{out},n}^{(j)}(t)$ for particular values of i, j, m and n. A simple concatenation, in which the components connect only to external fields, obeys equations of motion of the same form (21), with the following matrices:

$$\alpha = \begin{bmatrix} \alpha^{(1)} \\ \vdots \\ \alpha^{(n)} \end{bmatrix}, \quad A_{\text{NL}}(z,t) = \begin{bmatrix} A_{\text{NL}}^{(1)}(\alpha^{(1)}, t) \\ \vdots \\ A_{\text{NL}}^{(n)}(\alpha^{(n)}, t) \end{bmatrix},$$

$$\mathbf{A} = \begin{bmatrix} \mathbf{A^{(1)}} & 0 & 0 \\ 0 & \ddots & 0 \\ 0 & 0 & \mathbf{A^{(n)}} \end{bmatrix}, \quad \mathbf{a} = \begin{bmatrix} \mathbf{a^{(1)}} \\ \vdots \\ \mathbf{a^{(n)}} \end{bmatrix}, \quad \mathbf{B} = \begin{bmatrix} \mathbf{B^{(1)}} & 0 & 0 \\ 0 & \ddots & 0 \\ 0 & 0 & \mathbf{B^{(n)}} \end{bmatrix},$$

$$\mathbf{C} = \begin{bmatrix} \mathbf{C^{(1)}} & 0 & 0 \\ 0 & \ddots & 0 \\ 0 & 0 & \mathbf{C^{(n)}} \end{bmatrix}, \quad \mathbf{c} = \begin{bmatrix} \mathbf{c^{(1)}} \\ \vdots \\ \mathbf{c^{(n)}} \end{bmatrix}, \quad \mathbf{D} = \begin{bmatrix} \mathbf{D^{(1)}} & 0 & 0 \\ 0 & \ddots & 0 \\ 0 & 0 & \mathbf{D^{(n)}} \end{bmatrix} \tag{22}$$

Connections between components are modeled by splitting the I/O fields into "internal" (β^I) fields and "external" (β^E) fields, as follows:

$$\beta_{\text{in}} = P_{\text{in}} \begin{bmatrix} \beta_{\text{in}}^E \\ \beta_{\text{in}}^I \end{bmatrix}, \quad \beta_{\text{out}} = P_{\text{out}} \begin{bmatrix} \beta_{\text{out}}^E \\ \beta_{\text{out}}^I \end{bmatrix} \tag{23}$$

where P_{in} and P_{out} are permutation matrices. This is illustrated with the toy circuit in Figure 1. In this circuit, there are four components, four external fields (solid red lines) and three internal fields (dotted lines). These permutations allow $\mathbf{B}$, $\mathbf{C}$ and $\mathbf{D}$ to be written in block form that separates the their "internal" behavior from their

"external" behavior:

$$\begin{aligned}
\mathbf{B}P_{\rm in} &= \left[\begin{array}{cc}\mathbf{B}^E & \mathbf{B}^I\end{array}\right] \\
P_{\rm out}^T\mathbf{C} &= \left[\begin{array}{c}\mathbf{C}^E \\ \mathbf{C}^I\end{array}\right] \\
P_{\rm out}^T\mathbf{c} &= \left[\begin{array}{c}\mathbf{c}^E \\ \mathbf{c}^I\end{array}\right] \\
P_{\rm out}^T\mathbf{D}P_{\rm in} &= \left[\begin{array}{cc}\mathbf{D}^{EE} & \mathbf{D}^{EI} \\ \mathbf{D}^{IE} & \mathbf{D}^{II}\end{array}\right]
\end{aligned} \tag{24}$$

The internal fields are arranged so that $\beta^I_{{\rm out},k}$ connects to $\beta^I_{{\rm in},k}$. Making these connections is equivalent to imposing $\beta^I_{\rm in} = \beta^I_{\rm out}$. One can then solve for the internal fields and eliminate them. The equations of motion for the circuit become:

$$\begin{aligned}
\dot\alpha = &\left[\mathbf{A} + \mathbf{B}^I(1-\mathbf{D}^{II})^{-1}\mathbf{C}^I\right]\alpha \\
&+ \left[\mathbf{a} + \mathbf{B}^I(1-\mathbf{D}^{II})^{-1}\mathbf{c}^I\right] + A_{\rm NL}(\alpha) \\
&+ \left[\mathbf{B}^E + \mathbf{B}^I(1-\mathbf{D}^{II})^{-1}\mathbf{D}^{IE}\right]\beta^E_{\rm in} \qquad (25) \\
\beta^E_{\rm out} = &\left[\mathbf{C}^E + \mathbf{D}^{EI}(1-\mathbf{D}^{II})^{-1}\mathbf{C}^I\right]\alpha \\
&+ \left[\mathbf{c}^E + \mathbf{D}^{EI}(1-\mathbf{D}^{II})^{-1}\mathbf{c}^I\right] \\
&+ \left[\mathbf{D}^{EE} + \mathbf{D}^{EI}(1-\mathbf{D}^{II})^{-1}\mathbf{D}^{IE}\right]\beta^E_{\rm in} \qquad (26)
\end{aligned}$$

The nonlinear part of the stochastic equations, $A_{\rm NL}(\alpha)$, does not change. In other words, the only effect of interconnections is to renormalize the linear part of the input-output equations, as follows:

$$\begin{aligned}
\mathbf{A} &\to \left[\mathbf{A} + \mathbf{B}^I(1-\mathbf{D}^{II})^{-1}\mathbf{C}^I\right] \\
\mathbf{a} &\to \left[\mathbf{a} + \mathbf{B}^I(1-\mathbf{D}^{II})^{-1}\mathbf{c}^I\right] \\
\mathbf{B} &\to \left[\mathbf{B}^E + \mathbf{B}^I(1-\mathbf{D}^{II})^{-1}\mathbf{D}^{IE}\right] \\
\mathbf{C} &\to \left[\mathbf{C}^E + \mathbf{D}^{EI}(1-\mathbf{D}^{II})^{-1}\mathbf{C}^I\right] \\
\mathbf{c} &\to \left[\mathbf{c}^E + \mathbf{D}^{EI}(1-\mathbf{D}^{II})^{-1}\mathbf{c}^I\right] \\
\mathbf{D} &\to \left[\mathbf{D}^{EE} + \mathbf{D}^{EI}(1-\mathbf{D}^{II})^{-1}\mathbf{D}^{IE}\right]
\end{aligned} \tag{27}$$

An alternative approach to generating the $\mathbf{A},\mathbf{B},\mathbf{C},\mathbf{D}$ coupling matrices is to propagate backwards from a given component, accumulating amplitudes from other components, splitting into additional paths when needed, and terminating at external inputs. This method works well for circuits without loops, but may converge slowly if low-loss loops (effectively cavities without internal state) are present. The algebraic approach presented above is advantageous for such loop-containing circuits, such as those in Ref. [23]. Finally, it should be noted that instead of applying these circuit reduction rules, one can also work in a fully quantum picture and describe the whole network using SLH models [12]. In this case, the final overall network model leads to a master equation that leads to the same SDEs as above.

For circuits with fixed component parameters, the coupling matrices need to be computed only once at the beginning of the simulation. The computational difficulty of integrating the SDEs scales, at worst, quadratically with the number of resonators. However, for many circuits, the coupling matrices are sparse, and the scaling is expected to be nearly linear.

D. Implementation and Validity

In the remainder of this paper we shall present simulation results obtained using a model based on Eqs. 1-2 with $\psi_i = -\pi/2$ (this determines the rotation angle of the Wigner distribution plots). The program, implemented in Matlab, allows a circuit to be defined as a netlist (a list of components, their parameters and connections) which can include resonators, two-port beamsplitters, phase shifters, and compound components. Functions were written to flatten the netlist (expand compound components), and to use a back-propagation method to convert the netlist to a set of matrices $\mathbf{A},\mathbf{B},\mathbf{C},\mathbf{D}$ defining the stochastic differential equations. More recently, the algebraic approach described above has also been implemented, and the two methods have been shown to produce consistent results. Integration of the stochastic equations was performed using an Euler-Maruyama timestep, modified to use exponential terms for the internal resonator dynamics:

$$\begin{aligned}
\alpha_j[n+1] = &\alpha_j[n]e^{(-i\Delta_j - \kappa_j/2 - 2i\chi_j|\alpha_j[n]|^2)\delta t} \\
&+ \left(\sum_k A_{jk}\alpha_k[n] + \sum_k B_{jk}\beta_{{\rm in},k}[n]\right)\delta t
\end{aligned} \tag{28}$$

where $\beta_{{\rm in},k}[n]$ includes a deterministic time-varying drive field plus independent Gaussian random variables for each timestep with amplitude $\sigma = 1/(2\sqrt{\delta t})$ for both the real and imaginary components, obtained from `normrnd`. The timestep δt was set small enough that the spontaneous jump rates in single-resonator calculations appeared to be independent of δt. Typically $\delta t = 0.025/\max(\{\Delta_j,\kappa_j\})$ which equals 5×10^{-4} for the counter circuit discussed below.

To check the validity of our semiclassical equations, we compared results with those obtained from a full quantum simulation, using the Quantum Optics Toolbox (QOT) [24]. One type of comparison is to examine the spontaneous jump rates for a single, bistable Kerr resonator with a constant drive field. Fig. 2 shows example results for a two-port resonator with $\kappa_1 = \kappa_2 = \kappa/2$, driven through one input. In the very low-photon-number case (Fig 2a,b), the downward jump rates show fairly good agreement between the two methods, but the upward jump rates are quite different. This is not surprising given that, in its lower state, the resonator contains just ~ 2 photons, and thus the approximation made in dropping the third-derivative terms from the Fokker-Planck equations (see Sec. II B) is not expected to be valid. In a somewhat higher-photon-number case

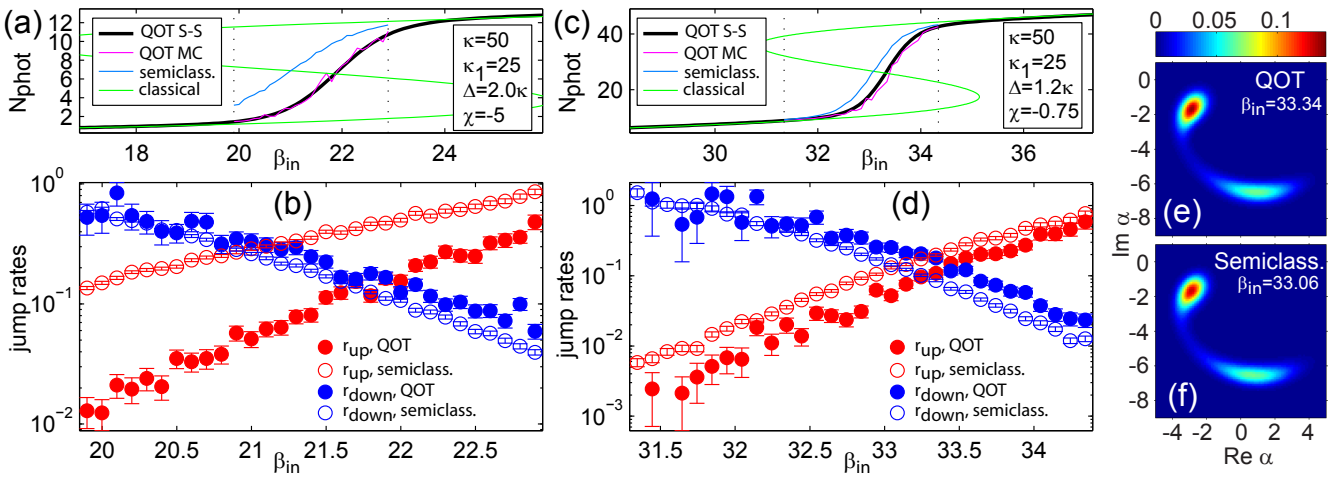

FIG. 2: (a) Time-averaged photon number vs. input field $\beta_{\rm in}$ as computed using the Quantum Optics Toolbox (QOT) [24] steady-state solution, QOT Monte-Carlo integration, our semiclassical approximation, and the classical formula, in a low-photon-number regime (parameters given in figure). (b) Upward (red) and downward (blue) jump rates estimated from QOT (solid) and semiclassical (empty circles) simulations. (c,d) Similar to (a,b), but in a higher photon-number regime, giving better agreement. (e,f) Time-averaged Wigner distributions from the QOT and semiclassical simulations, with $\beta_{\rm in}$ set to obtain equal upper and lower state occupations; all other parameters same as in (c,d)

(Fig 2c,d), the downward and upward rates both show good, though imperfect, agreement. The semiclassical results appear to be shifted horizontally from the QOT results by $\delta\beta_{\rm in} \sim 0.3$. For a third comparison in which the "on" state had ~ 95 photons (using $\Delta = 1.1\kappa$, $\chi = -0.3$), the jump-rate curves were again horizontally shifted, by $\delta\beta_{\rm in} \sim 0.35$ [27]. The time-averaged Wigner functions computed from the full-quantum and semiclassical simulations (Fig.2e,f) look quite similar, provided that $\beta_{\rm in}$ is set to give the same ratio of upper and lower state populations in each case.

We also compared spontaneous jump rates in the two-resonator latch circuit presented below (Sec. III D) for the QOT and semiclassical methods. For the QOT simulation we used the Hamiltonian and collapse operators given in Ref. [25] (Supp. Info). The results, included in Fig. 10, show good agreement between the full-quantum and semiclassical methods.

III. EXAMPLES

In this section we apply the simulation method described above to a set of optical circuits that could be of interest for switching and logic. In III A we investigate whether circuits composed only of beamsplitters, phase shifters, and resonators with an ideal Kerr nonlinearity can provide the gain and digital signal restoration needed for cascading. In III B-III E we introduce a set of building blocks that can be used for general-purpose combinatorial and sequential logic, and as an example application, in III F we simulate a 4-bit ripple counter containing 88 resonators.

A. Inverting and non-inverting amplifiers

Consider the amplifier circuit shown in Fig. 3a. This is similar to the circuit in Ref. [25], but is simpler since it uses the signal from only one resonator output. The input field $\beta_{\rm in}$ first interferes with a constant field β_c on a beamsplitter, which has amplitude transmission coefficient $\cos\theta$ and reflection coefficient $\sin\theta$ (the minus sign in the lower-left corner of the beamsplitter indicates which output has a minus sign for the reflected component). The output exiting to the right is $\beta_{\kappa 1} = \beta_{\rm in}\cos\theta + \beta_c \sin\theta$. This field then enters the first input of a two-port ring resonator. In this example we have not yet included intrinsic losses, so the total loss is the sum of the two coupling losses, $\kappa = \kappa_1 + \kappa_2$. The second resonator output passes through a phase shifter with phase ϕ that is chosen so that the output has a phase of approximately zero in the "high" state. This last component captures the necessity of controlling the phases between components. In an experimental realization, the phase shifter could correspond simply to a carefully chosen propagation length, or it could represent a tunable component. Whether or not active phase control is required depends on factors such as how reproducibly devices can be fabricated, and the amplitude of temperature fluctuations expected during circuit operation.

This circuit can function as either a non-inverting amplifier or an inverting amplifier, depending on the sign of the auxiliary field β_c. Example parameters for both cases are given in Table I. Suppose, first, that we work in non-inverting mode, and that the design input amplitudes to stage 0 are $\beta_{\rm in} = \{0, 10\}$. Since the beamsplitter is highly transmissive, it serves mainly to displace the

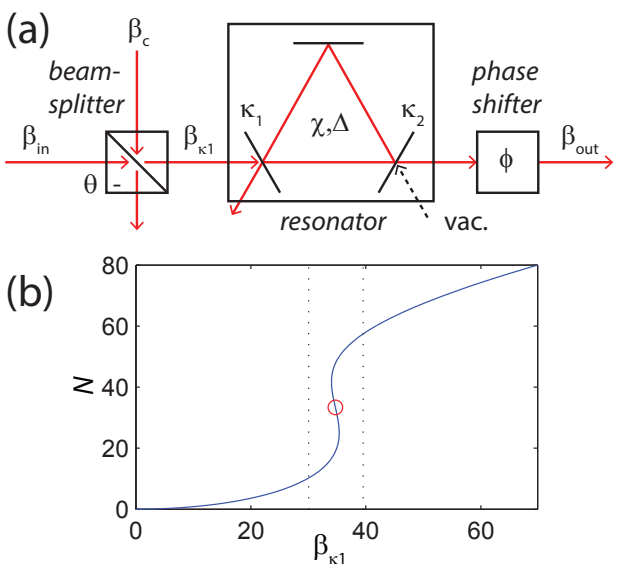

FIG. 3: (a) A simple amplifier circuit based on a nonlinear Kerr resonator. (b) Blue curve: Resonator photon number vs. resonator input field in the classical approximation, using the parameters from Table I. Dotted line: designed "low" and "high" input fields. Red circle: inflection point.

Amplifier Parameters				
stage	0	1	2	3
$t = \cos\theta$	$\sqrt{0.9}$	$\sqrt{0.9}$	$\sqrt{0.9}$	$\sqrt{0.9}$
$r = \sin\theta$	$\sqrt{0.1}$	$\sqrt{0.1}$	$\sqrt{0.1}$	$\sqrt{0.1}$
χ	-0.5	-0.5	-0.5	-0.5
κ_1	25	50	100	200
κ_2	25	50	100	200
Δ	50	100	200	400
Non-inverting				
design β_{in}	$\{0, 10\}$	$\{17, 37\}$	$\{26, 77\}$	$\{45, 145\}$
β_c	95	140	285	580
ϕ	-3.42	-3.42	-3.42	-3.42
Inverting				
design β_{in}	$\{0, 10\}$	$\{17, 37\}$	$\{32, 80\}$	$\{62, 163\}$
β_c	-125	-300	-607	-1215
ϕ	-0.2	-0.65	-0.74	-0.74

TABLE I: Simulation parameters used for the 4-stage non-inverting and inverting amplifiers.

field with little loss in amplitude, so that the field incident onto the resonator is $\beta_{\kappa 1} = \{30.04, 39.53\}$. The resonator then serves as a nonlinear filter, as represented by the blue curve in Fig. 3b, which is the steady-state solution to Eqs. 1-2 without the noise terms:

$$\kappa_1 |\beta_{\text{in},1}|^2 \approx n\left[(\kappa/2)^2 + (\Delta + 2\chi n)^2\right] \tag{29}$$

where $\beta_{\text{in},1}$ is the external field incident on one of the resonator inputs, $n \approx |\alpha|^2$ is the resonator photon number, and we have taken the limit $n \gg 1$. From this equation, one can show that classical bistability occurs for $\Delta > \frac{\sqrt{3}}{2}\kappa$, if $\chi < 0$. The red circle marks an inflection point in the RHS of the above equation, $n_{\text{inflection}} = -\frac{\Delta}{3\chi}$. The parameter values used in Fig. 3b are given in Table I (stage 0).

With these parameters, the nonlinear resonator is near the onset of bistability and exhibits a threshold-like response. The dotted lines in Fig. 3b represent the designed resonator field amplitudes for "low" and "high" inputs. The field exiting the resonator on the right has amplitude $\approx \sqrt{\kappa_2 n} \approx \{17, 37\}$ for low and high inputs, respectively, and thus the input field swing of 10 has been amplified by a factor of 2. A non-ideal feature of this simple circuit is that the low output is nonzero and has a different phase than that of the high output. The residual low output may cause complications when cascading components but can be eliminated by adding an interference path [25], as is included in the logic components introduced starting in III B.

Because of its threshold-like behavior, this amplifier has some digital signal restoration capability. Here, we perform simulations with a linearly varying triangle-wave input, with amplitude between 0 and 10, to examine whether the signal restoration, in the presence of quantum noise, is sufficient for cascading. For multiple stages, since each stage receives a larger input amplitude, the parameters for each amplifier stage must be chosen differently (Table I) to match the switching thresholds with the expected low and high resonator inputs. The simulated output field amplitudes of four cascaded inverting amplifiers are shown in Fig. 4a. We see that, despite the badly behaved input, the first stage (blue curve) has a clear switching behavior, although there is some variation in the output amplitude within the high and low states. In subsequent stages, the curves are quite flat in between switching events, and furthermore, the short-timescale noise due to quantum fluctuations does not appear to increase from one stage to the next. The corresponding output phases are plotted in Fig. 4b. The phase noise can be seen to decrease with each stage.

When performing these simulations, we noticed a markedly different behavior when we cascade inverting or non-inverting amplifiers. This can be seen most easily in the time-averaged complex field distributions of the resonators for the two cases, which are plotted in Figs. 5 and 6. The figures use a logarithmic scale in order to cover > 4 orders of magnitude, allowing the faint connections between the high and low states to be seen. In either case, in the first amplifier stage we see that the high state has a larger phase variation than the low state, which is a general feature for Kerr resonators even for constant inputs. In the inverting case, this noisier high state from the first stage leads to a low state in the second stage, which largely resets the noise. In the non-inverting case, the high state from the first stage leads to another high state in the second stage, allowing the phase noise

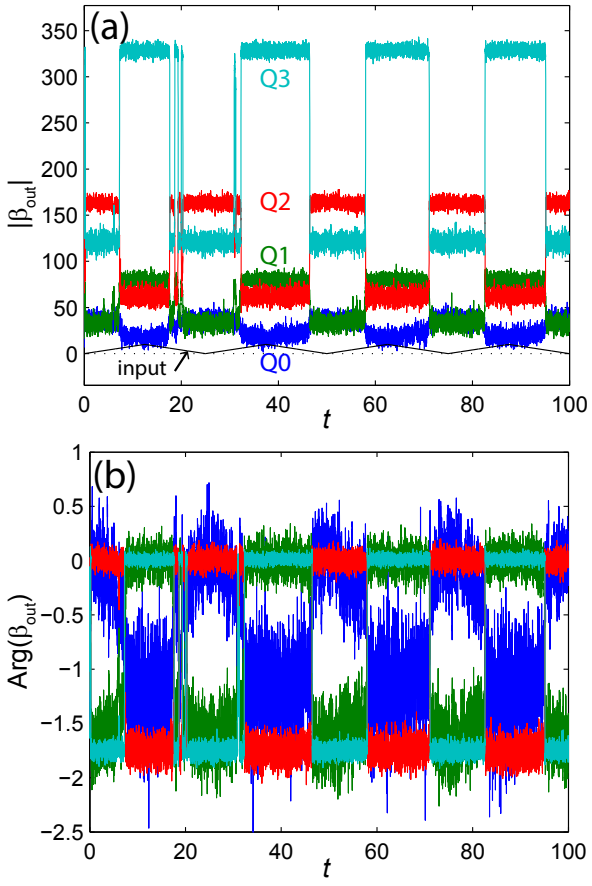

FIG. 4: (a) Simulated output amplitudes from stages 0, 1, 2, and 3 (labeled Q0, Q1, etc.) for four cascaded inverting amplifiers, using a triangle-wave input (black curve) with amplitude varying linearly between 0 and 10. The fields are averaged over a time interval of 0.01. (b) Corresponding output phases.

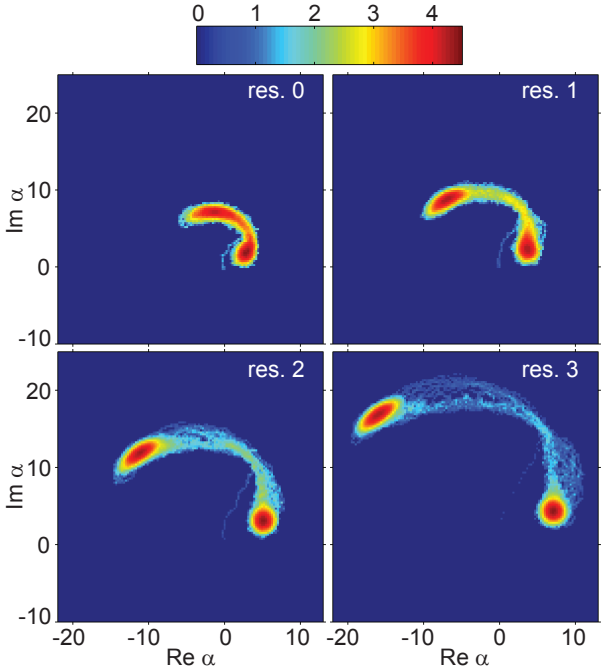

FIG. 5: Base-10 logarithm of the unnormalized, time-averaged distribution of the complex resonator fields in a four-stage inverting amplifier circuit, using a triangle-wave input.

to propagate further, even though it is diluted by the contribution of the next auxiliary coherent-state input. As a result, the phase noise in the last stage is larger for the non-inverting amplifiers, compared with the inverting amplifiers. If each amplifier is driven with a constant input, $\langle\beta_{\rm in}\rangle = 10$, after the fourth stage the phase noise amplitude of the non-inverting amplifier chain is 53% higher than for the inverting amplifier chain. This is part of the motivation for using inverting amplifiers in the fan-out circuits presented below.

B. AND gate

The first logic gate we consider is the AND gate shown in Fig. 7a. This is the same circuit that was shown in Fig. 1a of Ref. [25], except that here we include an intrinsic resonator loss, which will be unavoidable in practical photonic integrated circuits. Even if we have complete control over the resonator's output coupling rates, if we optimize for the lowest possible switching energy, then the intrinsic losses will be comparable to the coupling losses. Suppose, for example, that we design a gate to work near the onset of bistability, with $|\Delta| = \kappa$. The switching photon number will be close to the inflection point in the bistability curve, $n_{\rm switch} \approx |\Delta/(3\chi)|$. Using Eq. 29 for the input field $\beta_{\rm in}$, and setting the minimum switching energy (in photon units) to be $U_{\rm switch} \approx |\beta_{\rm in}|^2/\kappa$, we find,

$$U_{\rm switch} \approx \frac{\kappa^2}{|\chi|\kappa_1} \tag{30}$$

Setting $\kappa = 2\kappa_1 + \kappa_3$, where κ_3 is the intrinsic loss, and minimizing $U_{\rm switch}$ with respect to κ_1, we obtain $\kappa_3 = 2\kappa_1 = \kappa/2$, so that the intrinsic loss is half of the total loss. However, with such a large relative intrinsic loss, it is difficult to design circuits in which the output field amplitudes are as large as the input amplitudes. Thus, we have backed off from the optimum and used $\kappa_3 = 0.2\kappa$. The circuit parameters used to simulate the AND gate are given in Table II.

The AND gate works as follows: the two inputs interfere on a 50-50 beamsplitter. Only if both inputs are high (and in phase), the beamsplitter output is large enough to exceed the switching threshold of the resonator. We could simply use the output from resonator mirror 2 as the final output, as we did in the amplifiers discussed above. However, the performance can be improved by taking the output from resonator mirror 1, adjusting its phase, and interfering it with the output from resonator mirror 2 on a second beamsplitter. We adjust the phase

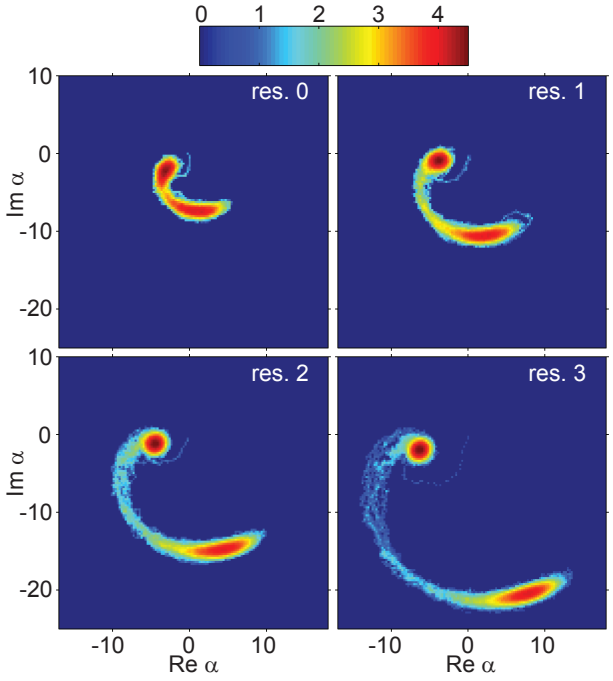

FIG. 6: Same as Fig. 5, but using non-inverting amplifier stages.

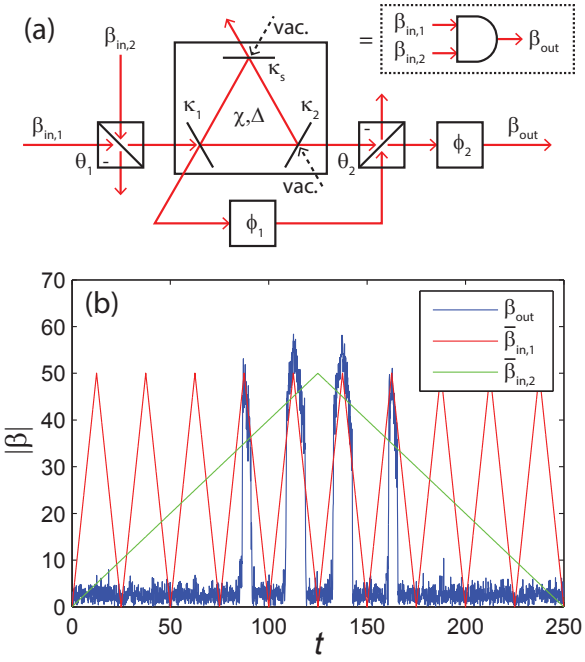

FIG. 7: (a) AND circuit based on a nonlinear Kerr resonator. (b) Simulated output field (blue) for triangle-wave inputs (red, green), with $E_{\rm high} = 50$. The fields are averaged over a time inverval of 0.01.

ϕ_1 and the mixing angle θ_2 so that, when only one of the circuit inputs is "high", the signals entering the second beamsplitter interfere destructively, giving a "low" output close to zero. The final phase shift ϕ_2 is chosen so that the "high" output has its phase close to zero.

Fig. 7b shows the simulated operation of the AND gate. Triangle waves are used to drive both inputs, to test the circuit's capability for digital signal restoration. The "high" output amplitude slightly exceeds the designed input "high" amplitudes. A separate simulation, in which the circuit was driven by a square-wave signal, indicates propagation delays (for the output to cross a level halfway between the steady-state low and high levels) ranging from $\tau = 0.023 = 1.2/\kappa$ for the fastest $\{1,1\} \rightarrow \{0,0\}$ input transition, to $\tau = 0.091 = 4.6/\kappa$ for the slowest $\{0,1\} \rightarrow \{1,1\}$ transition. Because of the direct path from the input to the output (through ϕ_1), the output can also exhibit short spikes if the inputs transition suddenly from $\{0,0\}$ to $\{1,0\}$.

C. Inverting fan-out

The AND gate described above has only a single optical output. Splitting this in two before sending it to other gates (such as more AND gates) would fail, since the amplitudes would be a factor of $1/\sqrt{2}$ smaller, and would be near or below the switching thresholds of the subsequent gates. Here we briefly introduce an inverting amplifier circuit that can be used both as a 2x fan-out, and as a NOT gate to complement the AND gate above, allowing for universal combinatorial logic.

	AND	Fanout	Latch
design $\beta_{\rm in}$	$\{0, E_{\rm high}\}$	$\{0, E_{\rm high}\}$	$\{0, E_{\rm high}\}$
β_c		$-2.6E_{\rm high}$	$1.75e^{-i\phi_1}E_{\rm high}$
χ	$-653.4/E_{\rm high}^2$	$-348.48/E_{\rm high}^2$	$-512.5/E_{\rm high}^2$
κ_1	20	20	20
κ_2	20	20	20
κ_3	10	10	10
Δ	50	50	50
$t_1 = \cos\theta_1$	0.707	0.707	0.707
$t_2 = \cos\theta_2$	0.89	0.89	0.629
$t_3 = \cos\theta_3$		0.707	0.829
ϕ_1	-1.39	-1.45	2.72
ϕ_2	2.65	-0.46	0.14
ϕ_3			2.34

TABLE II: Parameters used for the basic circuits. Here, $E_{\rm high}$ is the "high" level for external inputs. The simulations used $E_{\rm high} = 50$ (resonator photon number ~ 100) or $E_{\rm high} = 20$ (resonator photon number ~ 20).

Fig. 8a shows the inverting fan-out circuit, which is similar to the AND gate above, with a few differences. One of the inputs is replaced by a constant coherent drive which has a larger amplitude and is 180° out of phase with respect to the remaining input. The resonator nonlinearity is also decreased in order to increase the switching threshold. In an integrated photonics imple-

mentation, the per-photon nonlinearity could be changed most easily by varying the resonator length. The circuit parameters are given in Table II. As a result of these changes, the output field in the high state has sufficient amplitude that it can be divided in two at a final 50-50 beamsplitter, yielding two outputs with amplitudes slightly above the designed high level. Fig. 8b shows the simulated behavior of this circuit for a triangle-wave input, demonstrating the digital signal restoration capability of this circuit. For a square-wave input, the propagation delays (for mid-level crossing) are $\tau = 0.105 = 5.3/\kappa$ for the upward output transition and $\tau = 0.058 = 2.9/\kappa$ for the downward transition.

If fan-out to many outputs is required, one could design special circuits similar to the cascaded amplifiers described in III A. However, for the present demonstration, for simplicity we shall limit the number of primitive components, cascading the 2x fan-out as needed to create additional copies of a signal.

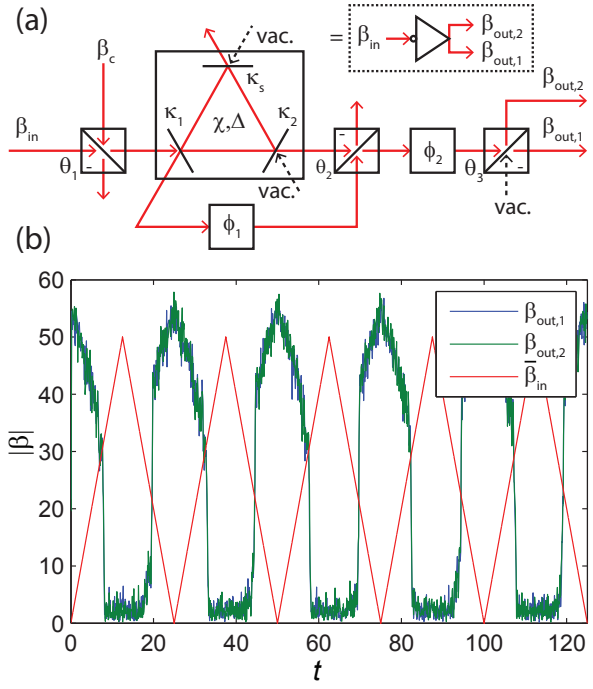

FIG. 8: (a) Inverting 2x fan-out circuit based on a nonlinear Kerr resonator. (b) Simulated output fields (blue, green) for a triangle-wave input (red), with $E_{\rm high} = 50$. The fields are averaged over a time inverval of 0.01.

D. Latch

To add memory to our circuits, we start with the $\overline{SR}$-NAND latch from Ref. [25]. The main change we made to the version shown in Fig. 9a was to incorporate intrinsic resonator losses, which required adjusting the other parameters (see Table II) so that the resonators operate closer to their switching thresholds. We might expect this to make the circuit more sensitive to noise.

The behavior of this circuit, simulated in Fig. 9b, can be understood as follows. Let us name the upper and lower resonators in the diagram resonators 1 and 2, respectively. If $\beta_{\rm reset}$ is high and resonator 1 is off, the coherent input β_c entering from the top of the diagram interferes constructively with $\beta_{\rm reset}$, so that the input to resonator 2 exceeds its switching threshold, keeping it in its "on" state. The feedback phase is chosen such that the κ_2 output of resonator 2, feeding back to the input of resonator 1, interferes destructively with the other inputs, keeping resonator 1 in its "off" state, independent of whether $\beta_{\rm set}$ is low (the "set" condition) or $\beta_{\rm set}$ is high (the "hold" condition). On the other hand, if $\beta_{\rm set}$ is high and $\beta_{\rm reset}$ is low (the "reset" condition), resonator 1 turns on and resonator 2 turns off. If $\beta_{\rm reset}$ then goes high again (the "hold" condition), resonator 1 stays on and resonator 2 stays off. Thus, in the "hold" condition, the system retains its previous state. The maximum propagation delay (for mid-level crossing) is $\tau = 0.11 = 5.5/\kappa$.

For $E_{\rm high} = 50$, resonator 1 contains approximately 0.5 photons in its undriven (set) state, 17 photons in its lower hold state, and 150 photons in its driven (reset) and higher hold states. The corresponding output field amplitudes are $\beta_{\kappa_2,1} \approx \sqrt{\kappa_2 n} \approx \{3, 18, 55\}$. The parameters of the final beamsplitter, which combines the outputs from the two resonators, and the associated phase ϕ_2, are chosen so that the final output is as close as possible to $E_{\rm high}$ whenever resonator 2 is in its high state, and as close as possible to zero otherwise.

When $E_{\rm high} \leq 25$, spontaneous jumps between the two bistable states of the "hold" condition occur with sufficient frequency to allow accurate estimation of the jump rate, as shown in Fig. 10. When $E_{\rm high} \leq 15$, this rate becomes too large to allow accurate state determination in between jump events, but we have extended the estimate to lower fields by fitting an exponential decay to the resonator field autocorrelation function. We should point out that, as $E_{\rm high} \to 0$ the semiclassical approximation is expected to become less and less accurate.

In solid-state implementations, our time units would likely correspond roughly to picoseconds, and thus an acceptable error rate for computing could be estimated as $< 10^{-18}$. By fitting a quadratic polynomial to the logarithm of the jump rate, and extrapolating to higher input fields, we estimate that $E_{\rm high} \approx 54$ would be required to achieve this, corresponding to ~ 177 photons contained within a resonator in its "on" state during the "set" condition (this corresponds to 35 aJ at $\lambda = 1\,\mu$m).

E. Type-D flip-flop

We next combine the primitive components defined above to make a clocked memory component that functions the same as the D flip-flop in electronics [26]. The circuit schematic is shown in Fig. 11a (see the previous

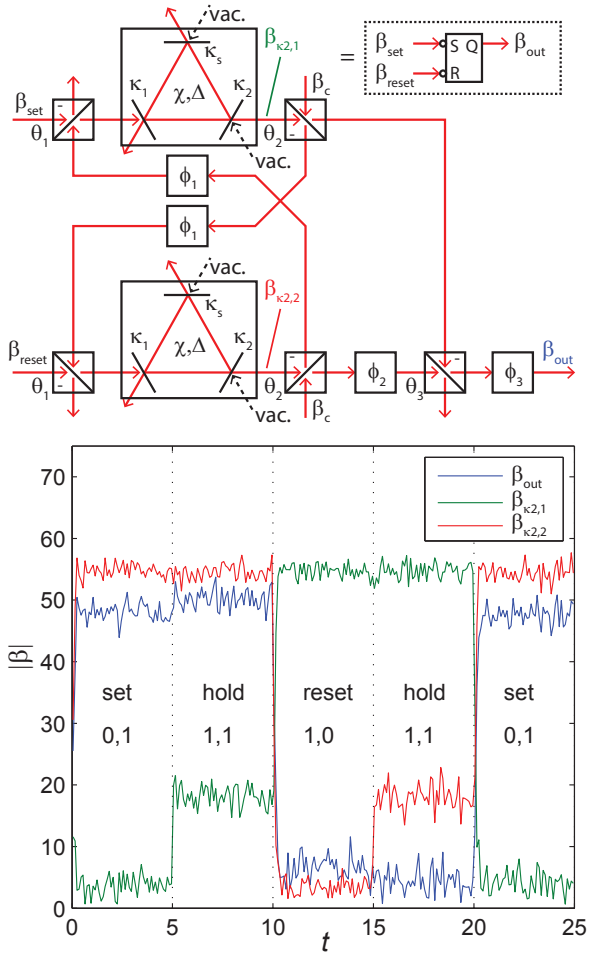

FIG. 9: (a) Latch circuit using two nonlinear Kerr resonators (see Ref. [25]). (b) Simulated final output field (blue), and the fields exiting from the κ_2 ports of resonators 1 and 2 (the upper and lower resonators in the diagram, respectively; green and red curves). For times in between the vertical lines, the two input levels are held constant at $\{0, 1\}E_{\rm high}$, as indicated, with $E_{\rm high} = 50$. The fields are averaged over a time inverval of 0.01.

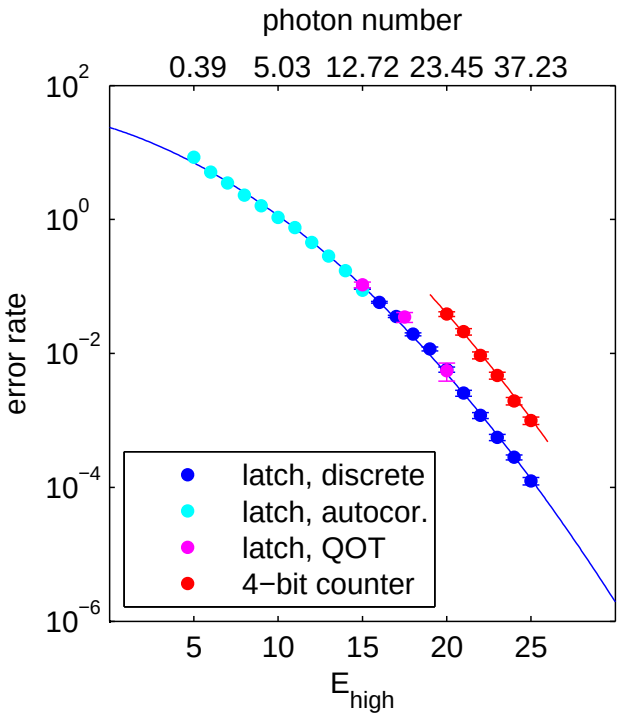

FIG. 10: Dark blue points: simulated spontaneous jump rates for a latch circuit in the "hold" condition, plotted as a function of the input field amplitude $E_{\rm high}$ (other circuit parameters are tied to $E_{\rm high}$ as described in Table II). The error bars assume Poisson statistics for the number of detected jumps. Cyan points: simulated jump rate in the low-field regime, estimated by fitting an exponential decay to the resonator field autocorrelation. Blue curve: quadratic fit to the logarithm of the jump rate. Magenta points: results obtained using the quantum optics toolbox [24, 25]. Red points: simulated jump rate for the 4-bit counter circuit. Red curve: same as the blue curve but multiplied by 8 (see text). The top x-axis indicates the mean photon number, corresponding to $E_{\rm high}$, for a resonator in its "on" state during the "set" condition.

figures for gate symbol definitions). This circuit is built around two $\overline{SR}$-NAND latches, denoted as "master" and "slave". The main input is denoted β_D, the clock is $\beta_{\rm clock}$, the intermediate "master" output is β_M, and the final "slave" output is β_Q. AND gates, with the clock or its compliment as one of the inputs, are used to control when the latches can change states. When the clock is high, β_D controls the state of the "master" latch, while the "slave" latch is frozen. When the clock goes low, the "master" latch is frozen, but its state is transferred to the "slave" latch. Numerous inverting fan-out gates are also required, either to divide or invert the various signals. Since these components account for more than half of the resonators in the circuit, replacing them with modified AND gates or improved amplifiers would be one of the more straightforward ways to optimize this circuit.

The simulated circuit dynamics are shown in Fig. 11b. For the first two input pulses (red), the rising edges occur when the clock (light blue) is already high, and thus the master latch (yellow) switches at the input rising edge. For the second two input pulses, the rising edges occur before the clock is high, and thus the master latch switches at the clock rising edge. The slave latch (dark blue) always transitions at the falling clock edge. Close examination shows that propagation delays (for mid-level crossing) of up to $\tau = 0.51 = 25.5/\kappa$ can occur following clock edges. This is approximately as one would expect from summing the individual component delays given above. For the slave transition, the path from the clock to the output passes through 4 fan-outs (with two upward and two downward transitions), an AND gate (upward), and a latch (can be upward). This circuit includes 20 resonators, 54 vacuum inputs, 16 non-vacuum coherent-state inputs, 54 beamsplitters, and 40 phase shifters. It is our first example of a circuit too

large to simulate using known full-quantum methods.

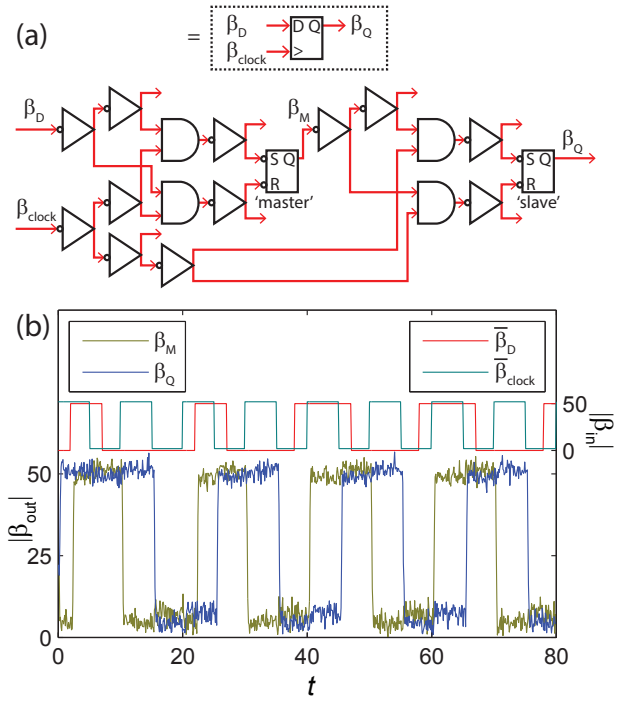

FIG. 11: (a) Schematic for a D flip-flop, built from the primitive circuits described above. (b) Simulated "master" output (yellow) and final "slave" output (dark blue) in response to the main input (red) and clock (light blue) square-wave signals. The simulation used $E_{\text{high}} = 50$, and the plotted fields are averaged over a time interval of 0.01.

F. 4-bit counter

As a simple application of the D flip-flop, here we demonstrate a 4-bit ripple counter. The circuit, shown in Fig. 12, contains 4 flip-flops, each representing one of the bits. The output of each flip-flop is inverted and fed back into its main input, causing its output state to toggle at each falling clock edge. Additionally, the output of a given flip-flop serves as the clock signal of the flip-flop representing the next-higher-order bit. Thus, two inverting fan-out components are required at each stage to generate the required copies.

When flattened into its primitive components, this circuit contains 88 resonators, 240 beamsplitters and 176 phase shifters, and requires 233 vacuum inputs and 72 non-vacuum inputs. The simulated behavior of the output fields is shown in Fig. 13. For $E_{\text{high}} = 50$, although the bit values start out with random values, the behavior for $t > 0$ is exactly as expected. However, for $E_{\text{high}} = 20$, random error events occur rather frequently. The estimated error rates for several values of E_{high} are plotted in Fig. 10. Since the counter circuit contains 8 latches, we expect the error rate to be at least 8 times larger than the error rate for a single latch. The good agreement between the counter error rates and the red curve in Fig. 13 (which is 8 times the fitted latch error rate) suggests that spontaneous jumps in the latch circuits under the "hold" condition are the most important error source in the counter circuit.

It is also interesting to look at the Wigner functions of the resonators to see if the quantum noise grows as signals propagate through such a large circuit. The time-averaged Wigner functions for two selected resonators are shown in Fig. 14. One of the resonators is in the first flip-flop, and the other is in the last flip-flop. The small-scale quantum noise does not appear to grow. This is not surprising, considering the digital restoration properties demonstrated above for the basic gates. Of course, large errors associated with quantum jumps between bistable states of a gate will propagate through the system, and we expect the overall error rate to scale linearly with the number of components.

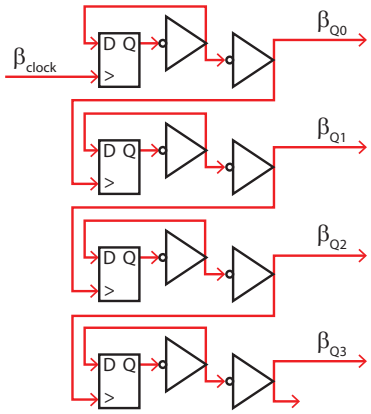

FIG. 12: Circuit diagram for a 4-bit ripple counter.

IV. OUTLOOK

We have demonstrated a simulation approach suitable for studying quantum noise in large-scale, nonlinear photonic circuits. We used this model to simulate a digital counter incorporating gates and latches based on previous designs. The results obtained so far suggest that the errors in the large-scale circuit are dominated by spontaneous jumps in the individual latches. From the error rates we extrapolate that the resonators within the latch circuit must contain ~ 180 photons in their "on" state to achieve acceptable error rates for computing. We consider this circuit design to be merely a starting point, and expect that systematic optimization will lead to designs that operate at lower energies and require fewer components. The existing model can also be used to study the sensitivity of circuit performance to random variations in the phases, coupling strengths and resonant frequencies of the primitive components that may result from

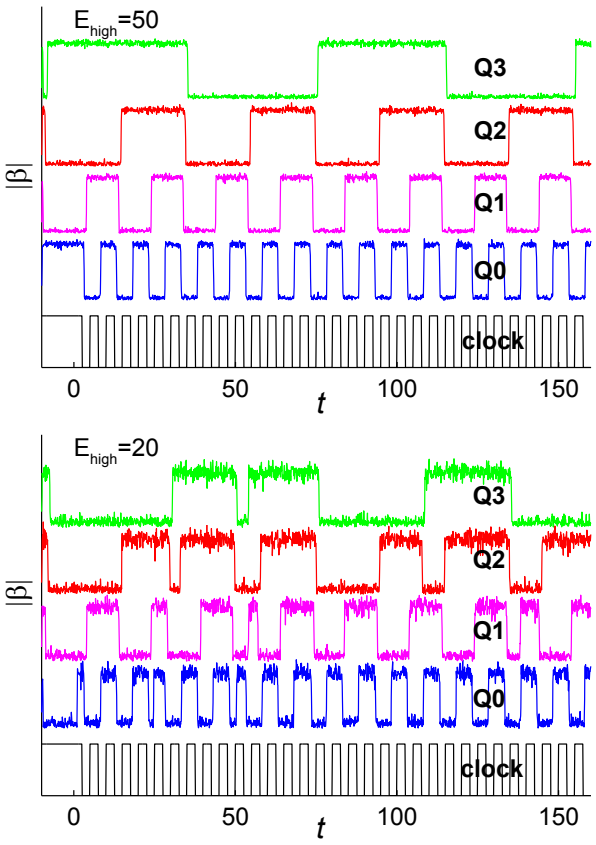

FIG. 13: Top: Simulated outputs of the 4-bit ripple counter for $E_{\text{high}} = 50$. Bottom: outputs for $E_{\text{high}} = 20$. The signals are averaged over a time interval of 0.1.

fabrication imperfections.

We plan also to increase the capabilities of our model in several ways. We have recently incorporated the semiclassical equations used here into the QHDL software framework [13], which will allow a single tool to perform both semiclassical and full-quantum simulations for a given circuit, and also allows for graphical construction of circuits. We also are working to expand the models to handle the quantum noise associated with non-ideal effects such as two-photon absorption, and other types of nonlinearities, such as carrier-based nonlinearities, which can be used to create either dispersive or absorptive bistability.

V. ACKNOWLEDGEMENTS

This work was supported by the Defense Advanced Research Projects Agency under Agreement No. N66001-12-2-4007.

[1] D. A. Miller, Nature Photonics **4**, 3 (2010).
[2] T. Tanabe, M. Notomi, S. Mitsugi, A. Shinya, and E. Kuramochi, Applied Physics Letters **87**, 151112 (2005).
[3] K. Nozaki, T. Tanabe, A. Shinya, S. Matsuo, T. Sato, H. Taniyama, and M. Notomi, Nature Photonics **4**, 477 (2010).
[4] K. Nozaki, A. Shinya, S. Matsuo, Y. Suzaki, T. Segawa, T. Sato, Y. Kawaguchi, R. Takahashi, and M. Notomi, Nature Photonics **6**, 248 (2012).
[5] J. S. Pelc, K. Rivoire, S. Vo, C. Santori, D. A. Fattal, and R. G. Beausoleil, Optics Express **22**, 3797 (2014).
[6] D. Ballarini, M. De Giorgi, E. Cancellieri, R. Houdré, E. Giacobino, R. Cingolani, A. Bramati, G. Gigli, and D. Sanvitto, Nature communications **4**, 1778 (2013).
[7] A. Faraon, I. Fushman, D. Englund, N. Stoltz, and J. V. Pierre Petroff, Nature Physics **4**, 859 (2008).
[8] R. Bose, D. Sridharan, H. Kim, G. S. Solomon, and E. Waks, Physical Review Letters **108**, 227402 (2012).
[9] W. Chen, K. M. Beck, R. Bücker, M. Gullans, M. D. Lukin, H. Tanji-Suzuki, and V. Vuletić, Science **341**, 768 (2013).
[10] Y.-D. Kwon, M. A. Armen, and H. Mabuchi, Physical review letters **111**, 203002 (2013).
[11] J. Kerckhoff, M. A. Armen, and H. Mabuchi, Optics Express **19**, 24468 (2011).
[12] J. Gough and M. R. James, Automatic Control, IEEE Transactions on **54**, 2530 (2009).
[13] N. Tezak, A. Niederberger, D. S. Pavlichin, G. Sarma, and H. Mabuchi, Philosophical Transactions of the Royal Society A: Mathematical, Physical and Engineering Sciences **370**, 5270 (2012).
[14] L. Bouten, R. van Handel, and A. Silberfarb, Journal of Functional Analysis **254**, 3123 (2008).
[15] H. Mabuchi, Physical Review A **78**, 015801 (2008).
[16] A. E. Nielsen, A. S. Hopkins, and H. Mabuchi, New Journal of Physics **11**, 105043 (2009).
[17] S. Carter, Physical Review A **51**, 3274 (1995).
[18] H. A. Haus and W. Huang, Proceedings of the IEEE **79**, 1505 (1991).
[19] C. Gardiner and M. Collett, Physical Review A **31**, 3761 (1985).
[20] C. Gardiner, A. Parkins, and P. Zoller, Physical Review A **46**, 4363 (1992).
[21] C. Gardiner and P. Zoller, *Quantum Noise: A Handbook of Markovian and Non-Markovian Quantum Stochastic Methods with Applications to Quantum Optics*, Springer Series in Synergetics (Springer, 2004), ISBN 9783540223016.

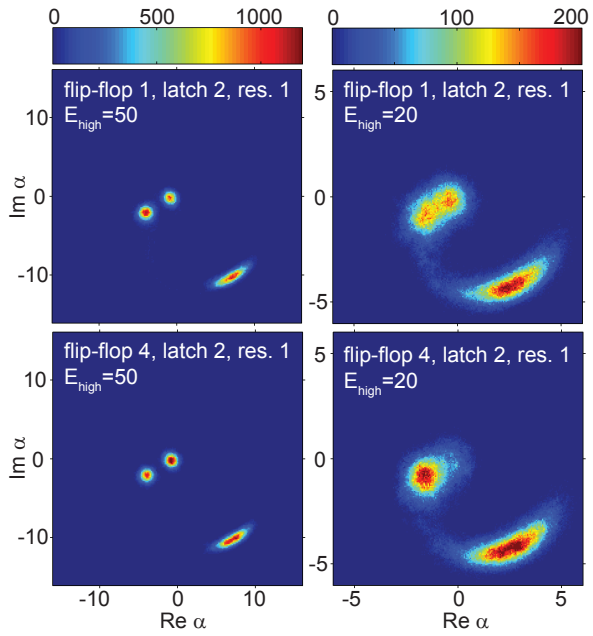

FIG. 14: For the 4-bit ripple counter, the time-averaged Wigner functions of the first resonator in the second latch of flip-flop 1 (upper-left) and flip-flop 4 (lower-left) for $E_{\rm high} = 50$; and the same for $E_{\rm high} = 20$ (upper-right and lower-right).

[22] M. O. Scully, M. S. Zubairy, and I. A. Walmsley, American Journal of Physics **67**, 648 (1999).

[23] K. Huybrechts, G. Morthier, and B. Maes, JOSA B **27**, 708 (2010).

[24] S. M. Tan, Journal of Optics B: Quantum and Semiclassical Optics **1**, 424 (1999).

[25] H. Mabuchi, Applied Physics Letters **99**, 153103 (2011).

[26] P. Horowitz, W. Hill, and T. C. Hayes, *The art of electronics* (Cambridge university press Cambridge, 1989).

[27] For these higher photon numbers, the Quantum Optics Toolbox function mcsolve had to be recompiled for double-precision arithmetic to give accurate results.